Supplemental Material:
Spinor self-ordering of a quantum gas in a cavity

Ronen M. Kroeze,[1,2,*] Yudan Guo,[1,2,*] Varun D. Vaidya,[1,2,3] Jonathan Keeling,[4] and Benjamin L. Lev[1,2,3]

[1]*Department of Physics, Stanford University, Stanford, CA 94305*
[2]*E. L. Ginzton Laboratory, Stanford University, Stanford, CA 94305*
[3]*Department of Applied Physics, Stanford University, Stanford, CA 94305*
[4]*SUPA, School of Physics and Astronomy, University of St Andrews, St Andrews KY16 9SS UK*

(Dated: September 19, 2018)

Cavity spectrum

The length of our cavity can be adjusted in situ using a slip-stick piezo [1]. The length in this work is set such that the $\mathrm{TEM}_{l,m}$ modes within $l+m=$ const. families [2] are resolvable but far separated in frequency from other mode families. Figure 1 shows the cavity spectra for the two experiments discussed in this paper. For experiments using the $\mathrm{TEM}_{0,0}$ mode, the cavity detuning is $\Delta_c = -4.00$ MHz, while $\tilde{\Delta}_c = -2.39$ MHz due to the dispersive shift (see the section on derivation of cavity-mediated spin-spin interaction below). Similarly, for the $\mathrm{TEM}_{1,0}$ mode, $\Delta_c = -0.96$ MHz and $\tilde{\Delta}_c = -0.79$ MHz. That is, the detuning is blue of the $\mathrm{TEM}_{0,1}$ mode, though red of the $\mathrm{TEM}_{1,0}$ mode. We observe dominant coupling to the $\mathrm{TEM}_{1,0}$ mode and no instability from proximity to the blue of the $\mathrm{TEM}_{1,0}$ mode. The splitting of approximately 50 MHz between adjacent families of modes is at least an order of magnitude larger than these detunings.

Frequency content

The frequency content of the laser beams is schematically summarized in Fig. 2. Both 780-nm Raman beams are derived from frequency-doubled 1560-nm light. The relative frequency between the two 1560-nm seed lasers

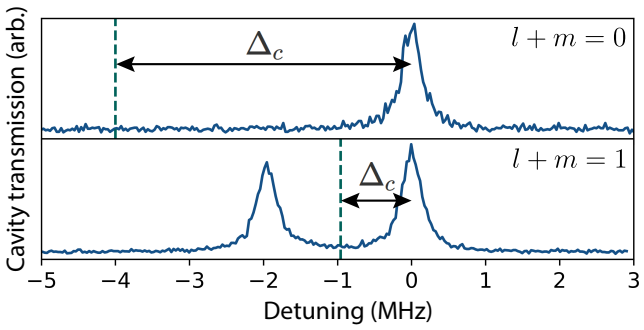

FIG. 1. Transmission spectra of the cavity in use, at the $l+m=0$ family and the $l+m=1$ family. The lock points are indicated by dashed lines, giving $\Delta_c = -4$ MHz and -0.96 MHZ for the experiments involving $\mathrm{TEM}_{0,0}$ and $\mathrm{TEM}_{1,0}$ respectively.

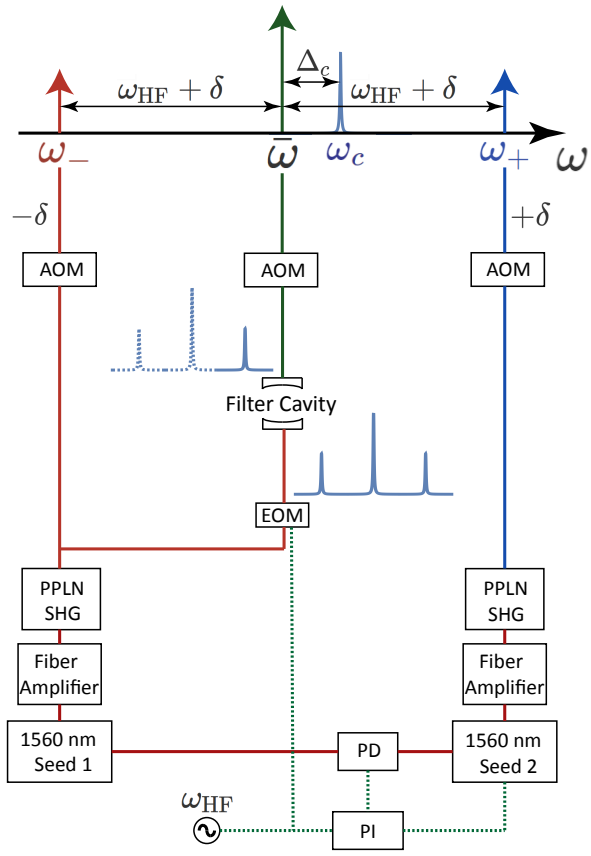

FIG. 2. Schematic for the laser system used in this experiment. Green lines represent electrical signals. The two 780-nm Raman beams are derived using second harmonic generation (SHG) from two 1560-nm fiber lasers, whose relative frequency is stabilized at ω_{HF} with a beat-note lock referencing seed 2 to seed 1. After SHG, the frequencies of the two doubled light beams are separated by $2\omega_{\mathrm{HF}}$. AOMs placed in the path of the beams allow for additional frequency adjustments and intensity control. The science cavity is stabilized at ω_c using 1560-nm light from seed 1 through the Pound-Drever-Hall (PDH) technique. The same rf source used to lock the fiber lasers is used to drive an electro-optic modulator (EOM) for the purpose of generating the local oscillator beam at ω_{LO}. The correct sideband is isolated by a filter cavity.

are stabilized with respect to a stable frequency source calibrated via microwave spectroscopy to oscillate at the frequency difference ω_{HF} between $|1,-1\rangle$ and $|2,-2\rangle$. ω_{HF} includes the Zeeman shift associated with the applied magnetic field. This frequency difference is controlled using a proportional-integral loop filter with feedback applied on seed 2. Additional 1560-nm light from seed 1 is used to stabilize the science cavity using the Pound-Drever-Hall (PDH) technique. The cavity resonance frequency ω_c is detuned from the $5^2S_{1/2}|2,-2\rangle$ to $5^2P_{3/2}$ transition by 154 GHz. The resulting Raman pump beams have atomic detunings of 160 and 147 GHz, resp. Using a fiber electro-optic modulator (EOM), sidebands at ω_{HF} are added onto the ω_- Raman beam in a separate path to derive the cavity probe (for use in taking the data in Fig. 1) and local oscillator beam. The drive signal to the EOM is split off from the same source that locks the seed lasers. We further isolate the correct sideband from the EOM output using a filter cavity; the resulting beam is at the mean frequency $\bar{\omega}$ of the two Raman beams and phase stable with respect to the cavity. Additional acousto-optic modulators (AOMs) provide intensity stabilization and additional frequency-shifting capabilities to symmetrically adjust the Raman detuning δ. All rf signals used in the experiment are stabilized with respect to the same 10-MHz Rb clock.

Holographic reconstruction

Above threshold, the superradiant cavity emission at frequency $\bar{\omega}$ observed on our EMCCD camera can have both amplitude and phase fluctuations in space. In the most general case, this field may be expressed as $E_c(\mathbf{r}) = |E_c(\mathbf{r})|e^{i\phi_c(\mathbf{r})}$. The amplitude and phase of this field is measured using a holographic technique based on the spatial Fourier demodulation analysis of the fringes of a spatial heterodyne measurement; see Ref. [3] for another recent demonstration of this technique. A large local oscillator (LO) beam at frequency $\bar{\omega}+\delta_{\mathrm{LO}}$ is incident on the EMCCD camera with a wavevector $\Delta\mathbf{k}$ relative to the cavity emission. This LO beam is derived from the output of the filter cavity in Fig. 2 and the AOM provides a controllable frequency shift δ_{LO}. The interference between the cavity emission $E_c(\mathbf{r})$ and the LO field $E_{\mathrm{LO}}(\mathbf{r})$ produces an image with an intensity $I_h(\mathbf{r})$ on the EMCCD camera; see Fig. 3(a). This may be expressed as

$$I_h(\mathbf{r}) = |E_c(\mathbf{r})|^2 + |E_{\mathrm{LO}}(\mathbf{r})|^2 + 2\chi(\delta_{\mathrm{LO}})|E_c(\mathbf{r})E_{\mathrm{LO}}(\mathbf{r})|\cos\left(\Delta\mathbf{k}\cdot\mathbf{r} + \Delta\phi(\mathbf{r})\right), \tag{1}$$

where $\Delta\phi(\mathbf{r}) = \phi_c(\mathbf{r}) - \phi_{\mathrm{LO}}(\mathbf{r})$ is the phase difference between the cavity and LO wavefronts. Both $|E_c(\mathbf{r})|$ and $\phi_c(\mathbf{r})$ are inferred from the amplitude and phase of the fringes produced by the oscillatory term of Eq. 1. Reduction of fringe contrast is characterized by the factor $\chi(\delta_{\mathrm{LO}})$. Several factors contribute to this reduction. For example, mismatch in the spatial and polarization-mode overlap of the cavity and LO reduces contrast. The contrast can also appear smaller due to a frequency difference between the LO and cavity emission: the fringe signals spatially average during the EMCCD camera's 2-ms integration time because the fringes have a non-zero phase velocity. This spatial averaging effect allows us to determine the cavity emission via measuring fringe contrast versus δ_{LO}, as shown in Fig. 3. Noise in the relative frequency between the cavity emission and LO also leads to spatial averaging.

In order to accurately extract $|E_c(\mathbf{r})|$ and $\phi_c(\mathbf{r})$, the image must first be corrected to account for intensity and phase variations of the LO beam. An independent measurement of the local oscillator intensity $I_{\mathrm{LO}}(\mathbf{r}) = |E_{\mathrm{LO}}(\mathbf{r})|^2$ allows us to create a corrected field image $E_{\mathrm{corr}}(\mathbf{r})$ whose fringe amplitude solely depends on $|E_c(\mathbf{r})|$:

$$\begin{aligned} E_{\mathrm{corr}}(\mathbf{r}) &= \frac{I_h(\mathbf{r}) - I_{\mathrm{LO}}(\mathbf{r})}{\sqrt{I_{\mathrm{LO}}(\mathbf{r})}} \\ &= \frac{|E_c(\mathbf{r})|^2}{|E_{\mathrm{LO}}(\mathbf{r})|} + 2\chi(\delta_{\mathrm{LO}})|E_c(\mathbf{r})|\cos\left(\Delta\mathbf{k}\cdot\mathbf{r} + \Delta\phi(\mathbf{r})\right). \end{aligned} \tag{2}$$

See Fig. 3(b) for plot of $E_{\mathrm{corr}}(\mathbf{r})$. Assuming the cavity field varies slowly over the fringe wavelength $2\pi/|\Delta\mathbf{k}|$, we may extract $|E_c(\mathbf{r})|$, shown in Fig. 3(c), and $\Delta\phi(\mathbf{r})$, shown in Fig. 3(d), by demodulating E_{corr} at the fringe wavevector $\Delta\mathbf{k}$.

Finally, the phase of the cavity field may be extracted from $\Delta\phi(\mathbf{r})$ by correcting for phase variations $\phi_{\mathrm{LO}}(\mathbf{r})$ of the local oscillator wavefront. The $\mathrm{TEM}_{0,0}$ mode of the cavity is used to calibrate these variations since it has a uniform phase over its transverse profile. Measuring $\phi_{\mathrm{LO}}(\mathbf{r})$ in this manner allows us to calculate the phase of the cavity wavefront as $\phi_c = \Delta\phi + \phi_{\mathrm{LO}}$ and consequently visualize the complex electric field of higher-order modes as shown in Fig. 4(b).

Spin-selective imaging

At the end of the experimental sequence, atoms can be in either $|\downarrow\rangle$, $|\uparrow\rangle$, or a superposition of the two. To selectively detect these states, we perform absorption imaging on the cycling transition between $5^2S_{1/2}|2,-2\rangle$ and $5^2P_{3/2}|3,-3\rangle$. Only the atoms in $|\uparrow\rangle$ are imaged due to the absence of repumping light. We verified that there is negligible depumping with circularly polarized light that drives purely σ_- transitions. Following this initial imaging pulse, an intense pulse of light resonant with the transition is applied, which results in the expulsion of the $|\uparrow\rangle$ population from view. Next, the atoms in $|\downarrow\rangle$ are transferred to $5^2S_{1/2}|2,-2\rangle$ using microwave adiabatic rapid passage and imaged using the same cycling transition. These atoms are subsequently also removed from the field of view, after which 'bright' and 'dark' images are taken for completing the absorption imaging process. The extracted optical densities from the first and second imaging pulse are then overlaid to produce spin-full absorption images such as those presented in Figs. 2(b), (c) and 4(b). The spherical scattering halos are due to two-body contact interactions.

Derivation of cavity mediated spin-spin interaction

The Hamiltonian of a single cavity mode a with spatial profile $\Xi(\mathbf{r})$ interacting with atoms can be written as in Ref. [4]:

$$H = \omega_c \hat{a}^\dagger \hat{a} + H_{\text{atom}} + H_{\text{trap}} + H_{\text{kinetic}} + H_{\text{int}}, \tag{3}$$

where ω_c is the optical frequency of the cavity mode, H_{atom} is the energy of the atomic internal states, and H_{trap} and H_{kinetic} capture the potential and kinetic energy of atoms in different internal states. H_{int} describes the coupling introduced by the pump beams (with optical frequency ω_+ and ω_-) and cavity:

$$\begin{aligned} H_{\text{int}} = &\int d^3\mathbf{r} \frac{1}{\sqrt{2}}\left(\Omega_+(\mathbf{r})e^{-i\omega_+ t} + \Omega_-(\mathbf{r})e^{-i\omega_- t}\right) \\ &\times \sum_{FF'} \left(\hat{A}^{+1}_{FF'}(\mathbf{r}) - \hat{A}^{-1}_{FF'}(\mathbf{r})\right) \\ &+ \int d^3 g_0 \Xi(\mathbf{r}) \hat{a} \sum_{FF'} \hat{A}^{0}_{FF'}(\mathbf{r}) + \text{H.c.}, \end{aligned} \tag{4}$$

where

$$\hat{A}^{(q)}_{FF'}(\mathbf{r}) = \sum_m c(F, m \to F', m+q) \hat{\psi}^\dagger_{F',m+q}(\mathbf{r}) \hat{\psi}_{F,m}(\mathbf{r}) \tag{5}$$

is the atomic raising operators connecting different hyperfine levels of the ground $\hat{\psi}_{F,m}$ and excited $\hat{\psi}_{F',m+q}$ states. The Clebsch-Gordon coefficients $c(F, m \to F', m+q)$ are the relative strengths of the transitions. We apply a bias magnetic field along $\hat{z}$. Both pump beams are linearly polarized along the cavity axis. The additional factor of $1/\sqrt{2}$ for the Rabi frequency of the two pump beams Ω_+ and Ω_- comes from the fact that the beams couple to both σ_+ and σ_- transitions, though only one is close to resonant for each beam due to Zeeman shifts.

The spatial profile of mode Ξ results in a spatially dependent single-photon Rabi frequency $g_0\Xi(\mathbf{r})/\Xi_{0,0}(0)$, where $\Xi_{0,0}$ is the profile of a $\text{TEM}_{0,0}$ mode. Given the large detunings of the pumps from the atomic excited states compared to the excited-state hyperfine splittings, all the excited states are assumed to be at the same energy ω_a. In the ground states, the Zeeman shift pushes $|F = 2, m_F = 0\rangle$ out of resonance, so we only consider the spin components $|F, m_F\rangle = |1,-1\rangle \equiv |\downarrow\rangle$ and $|F, m_F\rangle = |2,-2\rangle \equiv |\uparrow\rangle$ of the atom's hyperfine states as the coupled two-level system. All energy levels are defined with respect to the energy of $|\downarrow\rangle$, and the bare energy splitting ω_{HF} (hyperfine splitting plus additional Zeeman shift) between $|\uparrow\rangle$ and $|\downarrow\rangle$ is set by the bias magnetic field along $\hat{z}$ of ~ 2.82 G. We use microwave spectroscopy to calibrate the field and estimate a field fluctuation-induced frequency noise of 2.4 kHz on ω_{HF}.

To obtain the effective Hamiltonian, we transform Eq. 3 into a rotating frame defined by the unitary transformation $\hat{U} = \exp(-i\hat{H}_t t)$, where

$$\hat{H}_t = \frac{1}{2}(\omega_+ + \omega_-)\hat{a}^\dagger \hat{a} + \frac{1}{2}(\omega_+ - \omega_-) \int d^3\mathbf{r}\, \hat{\psi}^\dagger_\uparrow(\mathbf{r}) \hat{\psi}_\uparrow(\mathbf{r}). \tag{6}$$

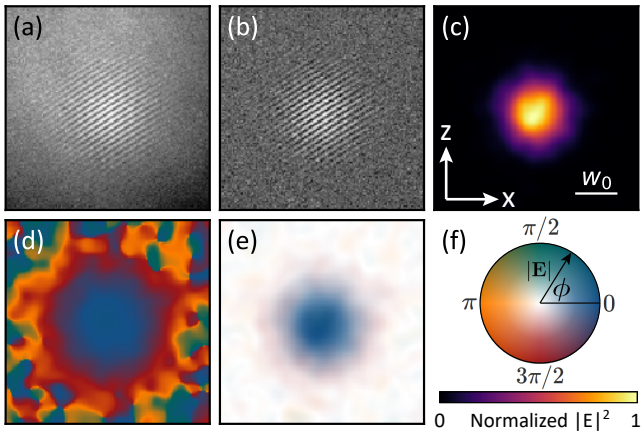

FIG. 3. Holographic reconstruction of cavity fields. (a) Camera image $I_h(\mathbf{r})$ generated by the interference between cavity emission from a $\text{TEM}_{0,0}$ mode and the local oscillator beam. (b) The corrected image $E_{\text{corr}}(\mathbf{r})$ generated from (a) using the procedure described in Eq. 2. (c) The intensity $|E_c(\mathbf{r})|^2$ of the cavity emission extracted from (b). (d) The phase of the cavity emission extracted from (b). (e) A visualization of the complex electric field constructed using the amplitude from (c) and phase from (d). (f) Color legend for panels (c) and (e). Color wheel is for panel (e) while color bar is for panel (c).

Here, the coupled spin-spatial atomic states are represented by the spinor $\hat{\psi}(\mathbf{r}) = [\hat{\psi}_\uparrow(\mathbf{r}), \hat{\psi}_\downarrow(\mathbf{r})]^\intercal$. Before writing the resulting Hamiltonian, we define the detunings Δ_+ and Δ_- from the atomic excited state for each of the Raman transitions, the detuning Δ_c of the mean pump frequency from the cavity frequency ω_c, and the two-photon detuning of the cavity-assisted Raman transition resonance δ as:

$$\begin{aligned}
\Delta_+ &= \omega_+ - \omega_a \\
\Delta_- &= \omega_- + \omega_{\mathrm{HF}} - \omega_a \\
\bar{\omega} &= \frac{1}{2}(\omega_+ + \omega_-) \\
\Delta_c &= \frac{1}{2}(\omega_+ + \omega_-) - \omega_c \\
\delta &= \frac{1}{2}(\omega_+ - \omega_-) - \omega_{\mathrm{HF}}.
\end{aligned} \tag{7}$$

We set $\delta \approx -10$ kHz, while the detuning for other allowed Raman processes, e.g., the coupling between $|\downarrow\rangle$ and $|F = 2, m_F = 0\rangle$, is on the order of a few MHz due to Zeeman splitting. After adiabatically eliminating the atomic excited states and ignoring the s-wave interaction and external harmonic trapping potential, the resulting Hamiltonian $H = H_\uparrow + H_\downarrow + H_{\mathrm{cavity}} + H_{\mathrm{Raman}}$ in the rotating frame is given by

$$\begin{aligned}
H_\uparrow &= \int d^3\mathbf{r}\hat{\psi}_\uparrow^\dagger(\mathbf{r})\Big[-\frac{\hat{\mathbf{p}}^2}{2m} + \left(\frac{\Omega_+^2}{6(\Delta_+ + \omega_{\mathrm{HF}})} + \frac{\Omega_-^2}{6\Delta_-}\right)\cos^2(k_r x) + \frac{[g_0\Xi(x,z)]^2}{\Delta_+}\cos^2(k_r y)\hat{a}^\dagger\hat{a} - \delta\Big]\hat{\psi}_\uparrow(\mathbf{r}) \\
H_\downarrow &= \int d^3\mathbf{r}\hat{\psi}_\downarrow^\dagger(\mathbf{r})\Big[-\frac{\hat{\mathbf{p}}^2}{2m} + \left(\frac{\Omega_+^2}{6\Delta_+} + \frac{\Omega_-^2}{6(\Delta_- - \omega_{\mathrm{HF}})}\right)\cos^2(k_r x) + \frac{[g_0\Xi(x,z)]^2}{\Delta_-}\cos^2(k_r y)\hat{a}^\dagger\hat{a}\Big]\hat{\psi}_\downarrow(\mathbf{r}) \\
H_{\mathrm{cavity}} &= -\Delta_c\hat{a}^\dagger\hat{a} \\
H_{\mathrm{Raman}} &= \int d^3\mathbf{r}\Big[\frac{\sqrt{3}g_0\Xi(x,z)\Omega_+}{12\Delta_+}\hat{\psi}_\uparrow^\dagger(\mathbf{r})\hat{\psi}_\downarrow(\mathbf{r})\hat{a}^\dagger\cos(k_r x)\cos(k_r y) + \frac{\sqrt{3}g_0\Xi(x,z)\Omega_-}{12\Delta_-}\hat{\psi}_\downarrow^\dagger(\mathbf{r})\hat{\psi}_\uparrow(\mathbf{r})\hat{a}^\dagger\cos(k_r x)\cos(k_r y) + \mathrm{H.c.}\Big],
\end{aligned} \tag{8}$$

where we have separated out the longitudinal dependence of the cavity mode and $k_r = 2\pi/\lambda$. In the regime of large cavity detuning Δ_c, the dynamics of the cavity mode is faster than other dynamics, and therefore we adiabatically eliminate the cavity mode to obtain an atom-only Hamiltonian. To do so, we define local spin operators

$$\begin{aligned}
\hat{\sigma}_z(\mathbf{r}) &= \left[\hat{\psi}_\uparrow^\dagger(\mathbf{r})\hat{\psi}_\uparrow(\mathbf{r}) - \hat{\psi}_\downarrow^\dagger(\mathbf{r})\hat{\psi}_\downarrow(\mathbf{r})\right]/2 \\
\hat{\sigma}_x(\mathbf{r}) &= \left[\hat{\psi}_\uparrow^\dagger(\mathbf{r})\hat{\psi}_\downarrow(\mathbf{r}) + \hat{\psi}_\downarrow^\dagger(\mathbf{r})\hat{\psi}_\uparrow(\mathbf{r})\right]/2.
\end{aligned} \tag{9}$$

The two cavity-assisted Raman couplings are set to have the same strength

$$\frac{\sqrt{3}g_0\Omega_-}{12\Delta_-} = \frac{\sqrt{3}g_0\Omega_+}{12\Delta_+} \equiv \eta, \tag{10}$$

allowing the effective Hamiltonian to be written as

$$\begin{aligned}
H_{\mathrm{eff}} = &\int d^3\mathbf{r}d^3\mathbf{r}'\frac{\eta^2}{\Delta_c}\Xi(x,z)\Xi(x',z')\times \\
&\cos(k_r x)\cos(k_r x')\cos(k_r y)\cos(k_r y')\hat{\sigma}_x(\mathbf{r})\hat{\sigma}_x(\mathbf{r}') \\
&+ \int d^3\mathbf{r}(\hat{H}_k - \delta)\hat{\sigma}_z(\mathbf{r}),
\end{aligned} \tag{11}$$

where

$$\begin{aligned}
\hat{H}_k = &-\frac{\hat{\mathbf{p}}^2}{2m} + \left[\frac{\Omega_+^2}{6(\Delta_+ + \omega_{\mathrm{HF}})} + \frac{\Omega_-^2}{6\Delta_-}\right]\cos^2(k_r x) \\
&- \left[\frac{\Omega_+^2}{6\Delta_+} + \frac{\Omega_-^2}{6(\Delta_- - \omega_{\mathrm{HF}})}\right]\cos^2(k_r x).
\end{aligned} \tag{12}$$

We have ignored the small Stark shift term proportional to $1/\Delta_{+,-}$ due to the cavity field. Our system therefore realizes a transverse-field Ising model of the form

$$\begin{aligned}
H_{\mathrm{Ising}} \propto &\sum J_{ij}\cos k_r x_i \cos k_r x_j \cos k_r y_i \cos k_r y_j \hat{\sigma}_x^i\hat{\sigma}_x^j \\
&+ h\hat{\sigma}_z^i,
\end{aligned} \tag{13}$$

with direct spin-spin interaction mediated through the cavity mode. We are able to describe the system with an effective Ising Hamiltonian because, unlike in Ref. [5], we operate in the large-Δ_c dispersive regime.

Mapping to the Dicke model

To understand the threshold at which organization occurs, it is useful to map our system onto a Dicke

model [6, 7]. The experiment begins with a condensate in $|\downarrow\rangle$ and when the cavity-mediated Raman process causes a spin flip, a momentum kick is also imparted onto the atoms. Within the single-recoil limit, the dynamics can be captured by two atomic modes

$$\begin{aligned}\hat{\psi}_\downarrow &= \hat{c}_\downarrow \psi_0 \\ \hat{\psi}_\uparrow &= \hat{c}_\uparrow \psi_1,\end{aligned} \tag{14}$$

where, for simplicity,

$$\begin{aligned}\psi_0 &= 1 \\ \psi_1 &= 2\cos(k_r x)\cos(k_r y).\end{aligned} \tag{15}$$

Since the pump lattice potential is retained in the Hamiltonian, the differential Stark shift on $\psi_\uparrow$ and $\psi_\downarrow$ due to the lattice beams has been taken into account. Taking advantage of the $\lambda = 2\pi/k_r$ periodicity along both the pump and cavity direction, shifting the energy of the $c_\downarrow$ mode to zero, and performing the integrals, the Hamiltonian is evaluated to be

$$\begin{aligned}H =& -\Delta_c \hat{a}^\dagger \hat{a} + \left\{ 2\omega_r + \frac{3}{4}\left[\frac{\Omega_+^2}{6(\Delta_+ + \omega_{\mathrm{HF}})} + \frac{\Omega_-^2}{6\Delta_-}\right] - \frac{1}{2}\left[\frac{\Omega_+^2}{6\Delta_+} + \frac{\Omega_-^2}{6(\Delta_- - \omega_{\mathrm{HF}})}\right] - \delta \right\} \hat{c}_\uparrow^\dagger \hat{c}_\uparrow \\ &+ \left[\frac{\sqrt{3}}{24}\frac{g_0\Omega_+}{\Delta_+}\hat{c}_\uparrow^\dagger \hat{c}_\downarrow + \frac{\sqrt{3}}{24}\frac{g_0\Omega_-}{\Delta_-}\hat{c}_\downarrow^\dagger c_\uparrow\right]\left(\hat{a}^\dagger + \hat{a}\right) + \frac{g_0^2}{2\Delta_-}\hat{c}_\downarrow^\dagger c_\downarrow \hat{a}^\dagger a + \frac{3g_0^2}{4\Delta_+}\hat{c}_\uparrow^\dagger c_\uparrow \hat{a}^\dagger a.\end{aligned} \tag{16}$$

The bare energy of the $c_\uparrow$ mode is shifted due to the differential Stark shift

$$\omega_S = \frac{3}{4}\left[\frac{\Omega_+^2}{6(\Delta_+ + \omega_{\mathrm{HF}})} + \frac{\Omega_-^2}{6\Delta_-}\right] - \frac{1}{2}\left[\frac{\Omega_+^2}{6\Delta_+} + \frac{\Omega_-^2}{6(\Delta_- - \omega_{\mathrm{HF}})}\right], \tag{17}$$

which is a dynamic quantity during the linear ramp of the Raman-beams' power. The Raman detuning δ is therefore chosen such that the bare energy of the $\hat{c}_\uparrow$ mode is always positive during the experiment sequence.

As mentioned above in Eq. 10, the Raman couplings are chosen to be equal, and in anticipation of standard Dicke model notation [8], we define this coupling as

$$\frac{\sqrt{3N}}{24}\frac{g_0\Omega_+}{\Delta_+} = \frac{\sqrt{3N}}{24}\frac{g_0\Omega_-}{\Delta_-} \equiv \eta_D, \tag{18}$$

where $N = \hat{c}_\uparrow^\dagger \hat{c}_\uparrow + \hat{c}_\downarrow^\dagger \hat{c}_\downarrow$ is the total number of atoms. We now define the collective pseudospin-1/2 operators

$$\begin{aligned}\hat{J}_z &= \frac{1}{2}(\hat{c}_\uparrow^\dagger \hat{c}_\uparrow - \hat{c}_\downarrow^\dagger \hat{c}_\downarrow) \\ \hat{J}_+ &= \hat{c}_\uparrow^\dagger \hat{c}_\downarrow \\ \hat{J}_- &= \hat{c}_\downarrow^\dagger \hat{c}_\uparrow,\end{aligned} \tag{19}$$

where the $\hat{\mathbf{J}}$ operate on the coupled pseudospin-1/2 spin-spatial degree of freedom. The Hamiltonian can then be rewritten as

$$\begin{aligned}H =& \left(-\Delta_c + \frac{Ng_0^2}{2\Delta_-}\right)\hat{a}^\dagger \hat{a} + (2\omega_r + \omega_S - \delta)\hat{J}_z \\ &+ \frac{\eta_D}{\sqrt{N}}(\hat{J}_+ + \hat{J}_-)(\hat{a}^\dagger + \hat{a}) \\ &+ \frac{N(2\omega_r + \omega_S - \delta)}{2} + \left(\frac{3g_0^2}{4\Delta_+} - \frac{g_0^2}{2\Delta_-}\right)\hat{c}_\uparrow^\dagger c_\uparrow \hat{a}^\dagger \hat{a}.\end{aligned} \tag{20}$$

The first term in the third line is simply a energy offset, while the second term can be ignored as long as the population of $\hat{c}_\uparrow^\dagger \hat{c}_\uparrow$ is small, which is consistent with the single-recoil limit. The Hamiltonian therefore realizes the Dicke model, and the usual threshold expression applies:

$$\eta_c = \frac{1}{2}\sqrt{(-\Delta_c + Ng_0^2/\Delta_-)(2\omega_r + \omega_S - \delta)}. \tag{21}$$

Note that unlike in Refs. [9–12], our Raman scheme does not produce (dynamical) spin-orbit-coupling because this excited motional state has zero net momentum. However, since all parameters of this Dicke model realization are tunable, dynamical phenomena such as chaos and limit cycles are observable [4, 8, 13–17].

Lattice calibration and Raman coupling balancing

We calibrate the lattice depth of pump beams by performing Kapitza-Dirac diffraction of the BEC [18] prepared in either $|\uparrow\rangle$ or $|\downarrow\rangle$. This also allows us to characterize the differential Stark shift in the experiment.

The retroreflection mirror shared by the pump beams is mounted on a translation stage. Measuring the lattice depth of the combined pump beams, we adjust the translation stage to match the phases of the pump lattices at the position of the atoms. We note that the beat length of the two pump lattices (separated in optical frequency by 13.6 GHz) is ∼5 mm, much larger than the atomic cloud size; therefore, small mechanical fluctuations from the mirror mount will not cause the lattice to become out-of-phase at the atoms.

To match each beam's coupling strength, we linearly ramp up the Ω_+ (Ω_-) beam intensity for atoms prepared in $|\downarrow\rangle$ ($|\uparrow\rangle$) while monitoring cavity emission. Above a certain pump strength, atoms are transferred to the other spin state with an accompanying brief cavity emission pulse. The long-lived superradiance we observe in the main experiments of the text is distinct from the brief cavity emission from this single-beam spin-flip situation [4]. The critical Raman coupling strength at which this pulse occurs is given by:

$$\eta_{c,\mathrm{single}} = \sqrt{\frac{\gamma\kappa}{2N}\left[1+\left(\frac{-\Delta_c+2\omega_r+\omega_S'-\delta}{\gamma+\kappa}\right)^2\right]}, \quad (22)$$

where κ is the cavity decay rate and γ is a phenomenological parameter describing the collective spin decay rate [4]. Since only one beam is involved, ω_S' denotes the differential Stark shift on $|\uparrow\rangle$ and $|\downarrow\rangle$ due to a single pump beam. Matching the threshold for a single-beam spin-flip then balances the two Raman coupling processes. We perform the calibration with $\tilde{\Delta}_c = -1.4$ MHz. This is significantly larger than the two-beam Stark-shift contribution, $2\omega_r + \omega_S' - \delta \approx 10$ kHz. Therefore, the additional Stark shift from the simultaneous presence of both beams does not alter the matching condition considerably.

Relevance to Mivehvar *et al.* [19]

Our experiment is very similar to that proposed in the recent theoretical study of Ref. [19]. Indeed, our observation confirms salient features of coupled spin-spatial organization as predicted in the aforementioned paper: $\lambda/2$ periodicity of condensate density and spatially varying relative condensate phase. However, some important differences exist. In particular, in Ref. [19], the authors considered a thermal equilibrium situation, in which the energy of a state determined its probability. In contrast, our experiment and the simulations in Ref. [19] correspond to the nonequilibrium steady state that can be reached by dynamics starting from an initial prepared state. Specifically, since the initial state involves spin-down atoms at zero momentum, this means subsequent dynamics always involves spin-down states with even multiples of recoil momentum and spin-up states with odd multiples. Despite this locking, there remains a single $\mathbb{Z}_2$ symmetry (the sign of the spin-up wavefunction) which is spontaneously broken at the transition. Since the numerical results in Ref. [19] were derived using imaginary time propagation with an initial spin-polarized state, their results are similar to those for the case of the nonequilibrium steady state.

In addition to the above, we note that Reference [19] termed the symmetry breaking effect as a 'disorder-induced' or 'order-by-disorder' transition. This was on the basis that the Raman field has a zero average. As such, one could consider this zero-average field-inducing spin-spatial order as analogous to random magnetic-field-induced order [20]. However, we prefer to view this transition as simply a type of polariton-condensation phase transition. That is, rather than regard the spatially varying vacuum cavity field as a disordered field that induces a transition, we prefer to reserve the term 'disorder-induced' for non-periodic potentials, and the term 'order-by-disorder' for situations that more closely match the original use of that term for either enhanced entropy due to order [21], or the quantum extension of that concept where order is driven by enhanced phase space for fluctuations that lower the energy [22].

---

* R.K. and Y.G. contributed equally to this work.

[1] A. J. Kollár, A. T. Papageorge, K. Baumann, M. A. Armen, and B. L. Lev, "An adjustable-length cavity and Bose-Einstein condensate apparatus for multimode cavity QED," New J. Phys. **17**, 43012 (2015).

[2] A. E. Siegman, *Lasers* (University Science Books, 1986).

[3] N. Schine, M. Chalupnik, T. Can, A. Gromov, and J. Simon, "Measuring Electromagnetic and Gravitational Responses of Photonic Landau Levels," (2018), arXiv:1802.04418.

[4] Z. Zhang, C. H. Lee, R. Kumar, K. J. Arnold, S. J. Masson, A. L. Grimsmo, A. S. Parkins, and M. D. Barrett, "Dicke-model simulation via cavity-assisted Raman transitions," Phys. Rev. A **97**, 043858 (2018).

[5] Z. Zhiqiang, C. H. Lee, R. Kumar, K. J. Arnold, S. J. Masson, A. S. Parkins, and M. D. Barrett, "Nonequilibrium phase transition in a spin-1 Dicke model," Optica **4**, 424 (2017).

[6] K. Baumann, C. Guerlin, F. Brennecke, and T. Esslinger, "Dicke quantum phase transition with a superfluid gas in an optical cavity," Nature **464**, 1301 (2010).

[7] D. Nagy, G. Kónya, G. Szirmai, and P. Domokos, "Dicke-Model Phase Transition in the Quantum Motion of a Bose-Einstein Condensate in an Optical Cavity," Phys. Rev. Lett. **104**, 130401 (2010).

[8] P. Kirton, M. M. Roses, J. Keeling, and E. G. D. Torre, "Introduction to the Dicke model: from equilibrium to nonequilibrium, and vice versa," (2018), arXiv:1805.09828.

[9] Y. Deng, J. Cheng, H. Jing, and S. Yi, "Bose-Einstein Condensates with Cavity-Mediated Spin-Orbit Coupling," Phys. Rev. Lett. **112**, 143007 (2014).

[10] L. Dong, L. Zhou, B. Wu, B. Ramachandhran, and H. Pu, "Cavity-assisted dynamical spin-orbit coupling in cold atoms," Phys. Rev. A **89**, 011602 (2014).
[11] B. Padhi and S. Ghosh, "Spin-orbit-coupled Bose-Einstein condensates in a cavity: Route to magnetic phases through cavity transmission," Phys. Rev. A **90**, 023627 (2014).
[12] F. Mivehvar and D. L. Feder, "Synthetic spin-orbit interactions and magnetic fields in ring-cavity QED," Phys. Rev. A **89**, 013803 (2014).
[13] C. Emary and T. Brandes, "Chaos and the quantum phase transition in the Dicke model," Phys. Rev. E **67**, 066203 (2003).
[14] M. J. Bhaseen, J. Mayoh, B. D. Simons, and J. Keeling, "Dynamics of nonequilibrium Dicke models," Phys. Rev. A **85**, 013817 (2012).
[15] A. Altland and F. Haake, "Quantum chaos and effective thermalization," Phys. Rev. Lett. **108**, 073601 (2012).
[16] A. Altland and F. Haake, "Equilibration and macroscopic quantum fluctuations in the Dicke model," New J. Phys. **14**, 073011 (2012).
[17] F. Piazza and H. Ritsch, "Self-Ordered Limit Cycles, Chaos, and Phase Slippage with a Superfluid inside an Optical Resonator," Phys. Rev. Lett. **115**, 163601 (2015).
[18] O. Morsch and M. Oberthaler, "Dynamics of Bose-Einstein condensates in optical lattices," Rev. Mod. Phys. **78**, 179 (2006).
[19] F. Mivehvar, F. Piazza, and H. Ritsch, "Disorder-Driven Density and Spin Self-Ordering of a Bose-Einstein Condensate in a Cavity," Phys. Rev. Lett. **119**, 063602 (2017).
[20] A. Niederberger, T. Schulte, J. Wehr, M. Lewenstein, L. Sanchez-Palencia, and K. Sacha, "Disorder-Induced Order in Two-Component Bose-Einstein Condensates," Phys. Rev. Lett. **100**, 030403 (2008).
[21] J. Villain, R. Bidaux, J.-P. Carton, and R. Conte, "Order as an effect of disorder," J. Phys (Paris) **41**, 1263 (1980).
[22] A. G. Green, G. Conduit, and F. Krüger, "Quantum Order-by-Disorder in Strongly Correlated Metals," Annu. Rev. Condens. Matter Phys **9**, 59 (2018).